Journal of Marine Science and Application (2026) 25: 458-472
https://doi.org/10.1007/s11804-025-00616-5

RESEARCH ARTICLE

Experimental Investigation on the Vibration Characteristics of a Laminated Cylindrical Shell Structure Made of Steel and Composite Materials

Jiang Xu[1], Jun Guo[1], Zhen Bao[1] and Xiaojun Zhao[1]

Received: 09 December 2024 / Accepted: 06 March 2025

Abstract

The vibration and noise reduction characteristics of submersibles have been extensively investigated. Composite materials have various applications in automotive, aerospace, and other fields because of their excellent damping, corrosion resistance, specific strength, and other properties. However, compared with steel, composites are still deficient in terms of stability, stiffness, and economy. Composites also present structural dynamic parameter properties that differ from those of steel structures, which limit their application on submarines. This study aims to improve the vibration and noise reduction performance of submarines and further enhance the application of composite materials in submarine vehicles. For this purpose, the structural design of a laminated reinforced cylindrical shell made of steel and composite materials is conducted, and a traditional form of steel comparative structure with equal mass and shape is designed to contrast with the laminated model. The modal characteristics reflect the inherent frequency features of a structure. By altering the natural frequency, the model can be shifted away from the excitation frequency, which avoids intense resonance and effectively suppresses sound radiation caused by resonance. Therefore, the characteristics of the two structures in terms of modal and damping are compared and explored through experiments and simulations. The results show that the relative error of the modal between experiment and computation does not exceed 6%. After replacing 40% of the mass of steel with carbon fiber, the first three orders of the intrinsic frequency of the structure are increased by more than 13%, the amplitude of the transfer function is reduced by 9.6%, and the damping is improved by more than 75%. Therefore, the vibration and noise reduction characteristics of submersibles have been improved.

Keywords Submarine vehicles; Laminated; Modal; Damping

1 Introduction

The emergence of underwater submersibles has greatly advanced humanity's exploration of the deep sea. To date, submersibles are widely used in education, scientific research, military, and tourism sectors with the introduction of composite materials. Compared with metal materials, composites offer clear advantages in terms of strength, vibration reduction, and corrosion resistance (Guo et al., 2023; Xie et al., 2023), which lead to their increasingly widespread application in submersibles. The industry has extensively examined the application of composites in submersibles and the vibration characteristics of these vehicles. In terms of experimentation, Wang et al. (2024a) conducted experimental research on the compressive dwell fatigue behavior of pressure hulls made of titanium alloy for deep-sea manned submersibles. This study provided guidance for the structural design of manned cabins in deep-depth transparent submersibles. Chen et al. (2009) experimentally investigated the impact of rubber coatings on the blast resistance performance of naval hulls. The results showed that the coating only slightly affected the low-frequency response but could mitigate the high-frequency response. With regard to numerical research, Wang et al. (2024b) analyzed the buckling behaviors under axial compression for cylindrical shells made of steel and composite materials. They also derived the theoretical formula of the linear elastic buckling for these shells. Feng et al. (2024) aimed to determine the damage accumulation and

Article Highlights

- A laminated reinforced cylindrical shell structure made of steel and carbon fiber and a steel contrast structure with equal mass were designed and fabricated to simulate the characteristics of the submarine segment.
- Vibration tests were conducted on the laminated structure and the steel structure separately to test and compare the modal characteristics and transfer functions of the two structures.
- Damping test experiments, along with the modal characteristic analysis of the structure, were conducted to compare and analyze the similarities and differences in the damping characteristics of the two structures, which helped summarize the rules.

✉ Jun Guo
18323832173@hrbeu.edu.cn

[1] Institute of Marine Engineering, Harbin Engineering University, Harbin 150001, China

extension of composite laminates under secondary impact. For this purpose, they combined experimental and finite element simulation analyses to investigate the damage and load–time curve after secondary impact. McCoy and Sun (1997) employed finite element simulation techniques incorporating fluid–structure interaction effects. Moreover, they conducted a dynamic response analysis of laminated cylindrical shell structures constructed from graphite/epoxy resin subjected to underwater explosive loads. Their results highlighted the significant impact of fluid–structure interaction effects on stress distribution in composite structures. Liu et al. (2000) used finite element numerical analysis methods combined with a modified DAA method to study the dynamic response of hull structures made of glass fiber composites under underwater explosion loads. Their results were compared with experimental findings, which showed good agreement between finite element calculations and experimental results. Theoretically, Kandasamy et al. (2016) summarized various active, passive, and hybrid vibration mitigation methods, which widely employed the principles of adjusting stiffness and damping for vibration control. Shifting the natural frequency of the structure outside a certain bandwidth of the excitation frequency can prevent harmful energy superposition at resonance frequencies while increasing the damping of the structure can effectively reduce resonance peaks by dissipating vibrational energy. Yin et al. (2025) achieved effective control of the overall system vibration response by modifying the structural configuration, which resulted in a shift of peak frequencies in the structural vibration spectrum. Jiang et al. (2024) adjusted the inherent stiffness of the structure by adding mass locally, which successfully reduced the radiated noise by 2–3 dB. Li et al. (2016) performed modal and vibration noise experiments using an underwater vehicle model, which clarified the relationship between natural frequencies and the peak frequencies of the vibration noise spectrum. By modifying the structural configuration, they effectively controlled underwater acoustic radiation. Moon et al. (2010) used FEM to analyze the buckling failure of pressure cylindrical shells made of filament-wound composites for underwater vehicles. The results of their analysis, which was conducted using the self-developed finite element program ACOS, were compared with experimental results. This comparison revealed an error range of 2% to 23% between the analysis based on the program and the test results. Du and Cui (2014), and Du (2017) presented a finite element analysis (FEA) on spherical shells made of high-strength steel considering material and geometric nonlinearity, an elastic–plastic stress–strain relationship, and the initial deflection of the shell during the manufacturing process. The results were confirmed by model collapse tests. Moreover, Wang et al. (2019) proposed a relevant calculation and design method for spherical hulls made of ultrahigh-strength steel for full-ocean-depth manned cabins by using a direct method by FEA. The author also developed a sphere model and conducted a hydrostatic pressure experiment, which realized verification among different method results. Song et al. (2024) analyzed the natural frequency response of the FG bio-composite plate within the framework of the newly developed refined higher-order shear deformation plate theory. In addition, the imperfection impact on frequency behavior was evaluated while considering three imperfection distribution patterns. Fathallah et al. (2015) optimized the layering design of different types of carbon fiber materials to minimize the buoyancy coefficient of elliptical pressure hulls made of composite materials for submersibles. Tang et al. (2019) and Li et al. (2020) investigated the acoustic radiation characteristics of composite shell structures based on composite shell theory. They studied the influence of elastic modulus and ply layup on structural radiation noise through numerical calculations and experimental methods. Moreover, a new semi-analytical method was proposed based on thin shell theory to analyze the free vibration characteristics of cylindrical shells with stepped thickness. This method is suitable for exploring the free vibration characteristics of cylindrical shells with stepped thicknesses under complex boundary conditions. It offers advantages such as good convergence, high computational accuracy, and simplified boundary condition simulation. Sun and Zou (2015) utilized a three-dimensional hydroelasticity method to analyze the vibration response characteristics during underwater navigation of a certain type of submersible. By solving the generalized coordinate responses of dry modes and the corresponding added mass of the surrounding water, they determined the correspondence between dry modal frequencies and wet resonant frequencies. Xu et al. (2011) used mechanical impedance theory to determine the mechanical impedance characteristics of pressure-resistant shells through FEA software modeling and simulation. Their analysis provided essential raw data and parameter inputs for the dynamic characteristic analysis of the entire system involving pipeline–elastic support–shell foundation. It also offered necessary theoretical guidance for system design and engineering installation. Chen and Dong (2023) strengthened external pressure vessels using the autofrettage approach to achieve an optimal balance between structural strength and weight. Zhang et al. (2022) designed a carbon fiber-reinforced polymer composite for full ocean depth applications, which not only reduces structural mass but also exhibits high hydrostatic load-bearing capacity. Lee et al. (2013) conducted an optimization study on the design loads of cylindrical shells made of composite sandwiches under hydrostatic external pressure. Structural buckling failure and material failure constraints were considered during the optimization calculations. Messager et al. (2022) used FEMs to perform layer optimization design on laminated cylindrical pressure hull struc-

tures made of composites for deep-sea submarines. This design aimed to improve the buckling resistance of the structure. Lopatin and Morozov (2015) employed the Galerkin method to perform a buckling analysis on cylindrical shells made of composite sandwiches with both ends clamped under uniform external pressure. The results were compared with those obtained from FEMs, which led to the derivation of an analytical formula for the critical load of the structure. Wu et al. (2023) modeled the submarine hull as a jointed conical-orthogonally stiffened cylindrical–spherical shell coupled with several circular plates. They also proposed an analytical method for the coupled shaft–submarine hull system. The hydrodynamic pressures acting on the rotor and the duct–stator system were considered single-point forces and multiple uniformly or non-uniformly spaced point forces acting on the shaft and the conical shell, respectively. The vibration displacements were analytically expanded with Fourier series in the circumferential direction. Ismail et al. (2023) investigated the buckling loading of imperfect steel spherical shells under external pressure, which presented a numerical calculation with a focus on the buckling behavior of imperfect shells subjected to external pressure. Bakshi and Chakravorty (2014) studied the first-ply failure of conoidal shells made of thin composites subjected to uniformly distributed load, which aimed to achieve high failure values. Walker and Smith (2003) described a technique for combining genetic algorithms with FEM to minimize the mass and deflection using a multi-objective approach. Ghandehari et al. (2024) examined the free vibration characteristics of coupled nested conical shells made of porous composite materials. Ghandehari et al. (2025) also assessed the vibration behavior of a novel shell structure, that is, nested dual conical shells, and a truncated conical shell under varying thermal conditions. Rezaiee-Pajand and Masoodi (2019) investigated the buckling and post-buckling behavior of plates and shells with an efficient triangular shell element having six nodes.

The excellent damping properties of composite materials will not only greatly enhance the acoustic stealth performance of underwater submarines but also offer good impact protection for the equipment inside the submarine (Zhao et al., 2025; Ma et al., 2024). However, the composite material itself cannot adjust the balance of strength and stiffness well. Moreover, the production cost of high-performance composite materials, such as titanium alloy and carbon fiber, is dozens of times higher than that of steel products of equal quality. These factors have led to a lower maturity of composite materials in the submarine application. In response, this study takes the amidship section of the submersible as a sample and designs a laminated structure model with material properties between steel and composite materials. The manufacturing cost of this structure is only 3–5 times that of an equal-quality steel structure. A comparative model of steel with equal mass and shape is designed to compare the difference with the ordinary steel structure. Moreover, the modal and damping characteristics of the two models are analyzed and discussed through simulation and experiment. This study provides technical references for the design of submarines in the aspects of acoustic stealth, vibration reduction, and impact resistance protection.

2 Structural design

Laminated research models and steel comparison models with equal mass were designed to compare the structural characteristics of laminated and steel models. Based on literature research (Zhao, 2023; Xu, 2020; Yu et al., 2011; Zhang et al., 2011; Yang et al., 2011a; Yang et al., 2011b; Du et al., 2024; Cheng et al., 2024) and considering structural test conditions, the primary dimensions of the models were determined to be 0.6 m in diameter and 1 m in length. Numerical calculations indicated that reducing rib spacing beyond 50 mm did not significantly improve structural strength and stability but significantly increased overall model mass. Consequently, rib dimensions were finalized at 8 mm × 32 mm, with a rib spacing of 50 mm and a model thickness of 5 mm, to achieve a balance between structural weight and strength.

During the design of the laminated model, the thickness of the steel structure portion of the shell was reduced to ensure equal mass with the steel comparison model after the carbon fiber layup. Numerical calculations showed that structural stability notably decreased when the steel shell thickness in the laminated model was below 3 mm. No significant improvement in strength was observed compared with the steel model at 4 mm thickness. Therefore, the final design of the laminated model included a 3 mm thickness for the steel shell portion and a 14 mm thickness for the external carbon fiber layup. The layup was applied using wet winding at orthogonal angles to the outer surface of the steel structure.

The ends of the model were designed flat to mitigate adverse effects from end effects during testing. The test assessed the midsection of the cylinder. Transition rings were installed at both ends of the shell to protect the central test section from external influences. Detailed model dimensions are provided in the following text.

2.1 Steel structure

Detailed structural parameters of the comparison model made of pure steel are shown in Table 1. The parameters are explained in Table 2.

Table 1 Basic data of the steel model m

D	L	d	t_0	t_1	t_2	t_d
0.6	1.0	0.05	0.005	0.016	0.034	0.05

Table 2 Explanation of parameters

D	L	d	t_0	t_1	t_2	t_d	t_c
Model diameter	Model length	Rib spacing	Midsection shell thickness	Transition ring 1 thickness	Transition ring 2 thickness	End flat thickness	Thickness of carbon fiber layup

The steel used for the model is Q235 steel, with a yield strength of 235 MPa. The ribs are made of rectangular steel, with a size of 8 mm × 32 mm and a rib spacing of 50 mm. The total mass of the model is 471 kg. Detailed material properties can be found in Table 3.

Table 3 Material of the steel cylinder model

Material	Density (kg/m^3)	Elastic (Pa)	Poisson ratio
Q235	7850	2.1×10^{11}	0.3

The structural characteristics of the model are shown in Figure 1.

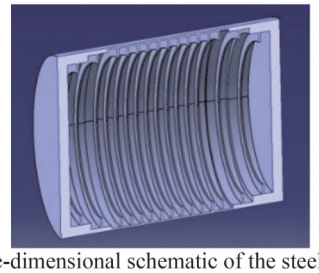

(a) Three-dimensional schematic of the steel structure

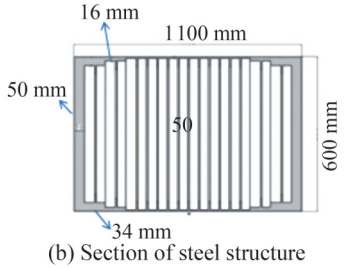

(b) Section of steel structure

Figure 1 Schematic of steel cylinder structure

2.2 Laminated structure

The laminated model involves laying a certain thickness of T700/M21 carbon fiber material on the external surface of the steel structure. The structural data for the laminated model are shown in Table 4, and the material data are shown in Table 5.

Table 4 Basic data of the laminated model m

D	L	D	t_0	t_c	t_1	t_2	t_d
0.6	1.0	0.05	0.003	0.014	0.016	0.034	0.05

The schematic cross section of laminated structure and steel structure is shown in Figure 2. In the figure, t denotes the thickness of the structure.

The main body material of the model is Q235 steel with a yield strength of 235 MPa. Rectangular steel ribs with dimensions of 8 mm × 32 mm are used. In the midsection, a carbon fiber layup of 14 mm thickness is applied at orthogonal angles, with each layer being 0.2 mm thick and totaling 70 layers. The total mass of the laminated model is 479 kg. The mass error between the laminated model and the steel model is shown in Table 6.

Table 5 Material properties of the laminated structure

Material	Density	Elastic/10^{10} (Pa)	Poisson ratio
		$E_1/E_2/E_3$	$P_{o12}/P_{o13}/P_{o23}$
T700	1600	5.5/5.5/1.0	0.045/0.250/0.250

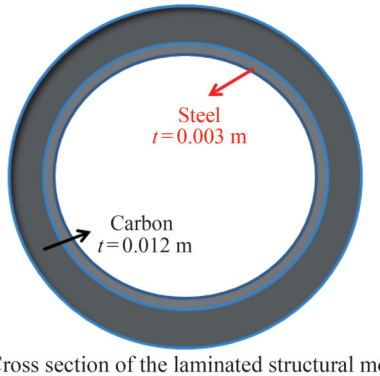

(a) Cross section of the laminated structural model

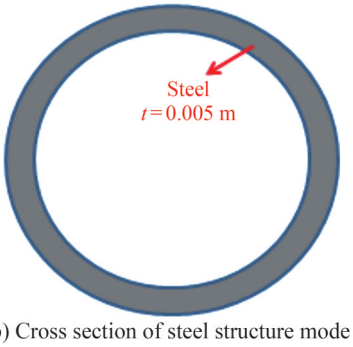

(b) Cross section of steel structure mode

Figure 2 Schematic cross section of laminated structure and steel structure

Table 6 Model mass error

Model mass		Relative error in model mass (%)
Steel structure model (kg)	Composite model (kg)	1.70
471	479	

Laminated models are constructed using the wet winding process. The wet winding process is a molding approach that uses a liquid resin system. In this process, continuous fiber

bundle roving or fiber cloth tape is first soaked with glue. Then, it is directly wound onto the surface of the core mold or liner under the control of fiber tension by the tension controller. Finally, the material is cured. This processing method ensures the product has good air tightness. The fiber alignment parallelism is outstanding, and the resin glue also provides a level of protection against fiber abrasion.

2.3 Comparison

Compared with the steel model, the laminated model reduces the steel mass in the midsection of the cylinder by 40% by replacing it with carbon fiber material. Given that the structural intrinsic frequency is related to the stiffness K and mass M, the structural stiffness is determined by the elastic modulus E and moment of inertia I. As shown in Tables 1–5, the ratio of the elastic modulus of steel and carbon fiber is $E_S/E_C = 3.82$, and the ratio of the moment of inertia of the 2 mm steel ring and the 14 mm carbon fiber ring is $I_S/I_C = 1/7.21$. Therefore, $E_S I_S = 0.53 E_C I_C$; that is, the laminated model stiffness should be higher than that of the steel model.

The structural mass of the two models is compared in Table 6.

Table 6 shows that the relative error in model mass is 1.7%, which is less than 2%. Considering that the laminated model has end fittings, the actual mass of the cylinder section should be slightly less than the data in Table 2. Given that the mass of the fittings is 2.4 kg, the actual mass error of the cylinder section is approximately 1.19%. Therefore, the two models can be assumed to have the same mass. Considering that the laminated model is stiffer than the steel model, the laminated model should have a higher intrinsic frequency than the steel model with equal mass.

The structural characteristics of the model are shown in Figures 3 and 4.

In Figure 3, t_s denotes the thickness of the steel structure, while t_c denotes the thickness of the carbon fiber.

In this work, experimental and numerical analyses will be conducted to investigate the modal and damping characteristics.

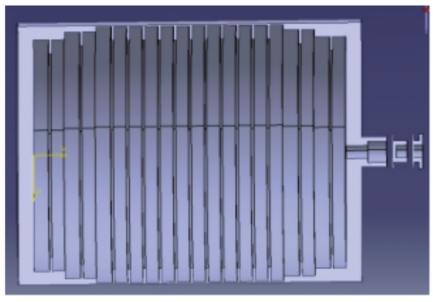

(a) Three-dimensional schematic of the laminated structure

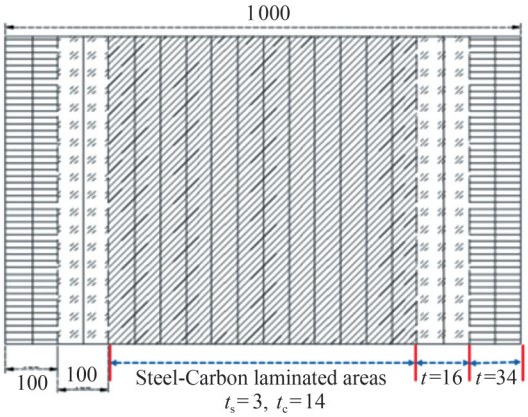

(b) Structural expansion diagram (physics) (units: mm)

Figure 3 Schematic of laminated cylinder structure

Figure 4 Physical models (Laminated model on the left, steel model on the right)

2.4 Numerical modeling process

In this study, the numerical modeling and analysis is conducted using the ABAQUS numerical analysis software developed by Dassault Systèmes France. The effectiveness of this method for calculating the modal and underwater shock response of the model has been verified in the existing literature (Szturomski and Kiciński, 2017; Amirabadi and Ghazangian, 2018). The emphasis here is on the process of creating and analyzing the laminated model.

Referring to the modeling method in the references (Zhao, 2023; Zhang et al., 2021), the steel part of the laminated structure is modeled by "solid" elements with mesh type C3D8R, while the composite part is modeled by "shell" elements. These elements are created using the outer surface of the created solid part, with cell type "S4R", and peeled off from the solid part. The material properties of both parts are created in the "Property" module, which is shown in Figures 5 and 6.

Notably, the combination of the two is realized in the "Create Composite Layup" function in the "Property" module. In this function, "Region", "Material", "Thickness", and "Rotation Angle" can be set for each layer of the laminated structure. The module defaults to a "Tie" connection between two neighboring layers, which ignores the relative displacement of the layers under external forces. This negligence is a limitation of this method.

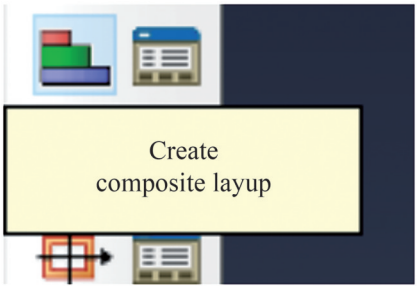

Figure 5 "Create Composite Layup" in the property module

		Ply name	Region	Material	Thickness	CSYS	Rotation angle	Integration points
1	✔	²Ã-1	POSITELAYUP-	T700/M21_2	0.0002	<Layup>	90	3
2	✔	²Ã-2	POSITELAYUP-	T700/M21_2	0.0002	<Layup>	0	3
3	✔	²Ã-3	POSITELAYUP-	T700/M21_2	0.0002	<Layup>	90	3
4	✔	²Ã-4	POSITELAYUP-	T700/M21_2	0.0002	<Layup>	0	3
5	✔	²Ã-5	POSITELAYUP-	T700/M21_2	0.0002	<Layup>	90	3
6	✔	²Ã-6	POSITELAYUP-	T700/M21_2	0.0002	<Layup>	0	3
7	✔	²Ã-7	POSITELAYUP-	T700/M21_2	0.0002	<Layup>	90	3
8	✔	²Ã-8	POSITELAYUP-	T700/M21_2	0.0002	<Layup>	0	3

Figure 6 Carbon fiber layup parameters of laminar numerical model

The modal analysis of the structure is conducted using the "frequency" function option in the "Linear Perturbation" option of the "Step" module. This module has a high level of application maturity, the description of which will be mentioned later.

The longitudinal wave velocity of steel is 5 500 m/s, and the analyzed frequency band of the model is predicted to be approximately 1 000 Hz at maximum. Thus, the wavelength should be not less than 5.5 m. This study will ensure that each wavelength contains at least 50 computational grids to ensure the accuracy of the calculation. Accordingly, the mesh size is set to 0.1 m.

3 Modal analysis

The experimental modal analysis aims to obtain modal shapes through experimental methods and determine the modal vectors of the response of the structural system. The process of experimental modal analysis generally involves capturing the time histories of excitation and response through experiments, applying digital signal processing techniques to obtain transfer functions or impulse response functions, and distinguishing modal parameters. For undamped and proportionally damped systems, the modal vectors representing the principal modes of the system are expressed using real numbers, which are referred to as real modal systems. By contrast, systems with structural damping or general viscous damping belong to complex modal systems. This study conducts a comparative analysis of the modal characteristics of the two models using experimental modal analysis methods.

3.1 Experimental principles

The motion differential equations for a multi-degree-of-freedom vibration system can be expressed as

$$\boldsymbol{M}\ddot{\boldsymbol{x}}(t) + \boldsymbol{C}\dot{\boldsymbol{x}}(t) + \boldsymbol{K}\boldsymbol{x}(t) = \boldsymbol{F}(t) \tag{1}$$

In the equation, $\boldsymbol{M}$ represents the mass matrix, $\boldsymbol{C}$ represents the damping matrix, $\boldsymbol{K}$ represents the stiffness matrix, $\boldsymbol{F}(t)$ represents the load force vector, and $\boldsymbol{x}(t)$ represents the displacement vector.

In conducting Fourier transform on the physical model, we let $\boldsymbol{x}(t) = \boldsymbol{X}\mathrm{e}^{\mathrm{j}\omega t}$ and $\boldsymbol{F}(t) = \boldsymbol{F}\mathrm{e}^{\mathrm{j}\omega t}$. When they are substituted into Equation (1), we obtain

$$\boldsymbol{X}(t) = \boldsymbol{H}(\omega)\boldsymbol{F}(t) \tag{2}$$

The transfer function is defined as

$$\boldsymbol{H}(\omega) = \left(\boldsymbol{K} - \omega^2\boldsymbol{M} + \mathrm{j}\omega\boldsymbol{C}\right)^{-1} \tag{3}$$

We suppose $\boldsymbol{\varphi}_r$ is the r-th order modal shape (eigenvector). Then, the transfer function matrix can be expressed as

$$\boldsymbol{H}(\omega) = \sum_{r=1}^{n} \frac{\boldsymbol{\varphi}_r\boldsymbol{\varphi}_r^{\mathrm{T}}}{\left(\boldsymbol{k}_r - \omega^2\boldsymbol{m}_r + \mathrm{j}\omega\boldsymbol{c}_r\right)} \tag{4}$$

Here, $\boldsymbol{m}_r$, $\boldsymbol{k}_r$, and $\boldsymbol{c}_r$ represent the r-th order modal mass matrix, modal stiffness matrix, and modal damping matrix, respectively. Each element of $\boldsymbol{H}(\omega)$ can be expressed as

$$\boldsymbol{H}_{ij}(\omega) = \sum_{r=1}^{n} \frac{\varphi_{ir}\varphi_{jr}}{\left(\boldsymbol{k}_r - \omega^2\boldsymbol{m}_r + \mathrm{j}\omega\boldsymbol{c}_r\right)} \tag{5}$$

Its physical meaning is the transfer function from excitation at point i to response at point j. For any row of the transfer matrix, we have

$$\left[\boldsymbol{H}_{i1}, \boldsymbol{H}_{i2}, \cdots, \boldsymbol{H}_{in}\right] = \sum_{r=1}^{n} \frac{\varphi_{ir}}{\left(\boldsymbol{k}_r - \omega^2\boldsymbol{m}_r + \mathrm{j}\omega\boldsymbol{c}_r\right)}\left[\varphi_{1r}, \varphi_{2r}, \cdots, \varphi_{nr}\right] \tag{6}$$

Evidently, each row of the transfer function matrix contains all modal parameters, which correspond to the r-th order modal shape. Therefore, when vibration signals are collected at a fixed measurement point on the test structure and all measurement points are sequentially excited, one row of the transfer function matrix can be obtained. Accordingly, all other modal analysis parameters can be derived. Similarly, when a specific point is excited and vibration responses at all points are measured, all modal parameters can be acquired.

3.2 Experimental conditions

The experiment employs transient excitation using a single-point hammer to conduct modal testing on the lami-

nated model and the steel comparison model. Multiple vibration accelerometers are used to record vibration acceleration responses at typical structural assessment points. Modal shapes and natural frequency distributions of different structures are derived through modal testing and analysis using the LMS Testlab modal testing module. The principles and procedures of the experiment are illustrated in Figures 7 to 9.

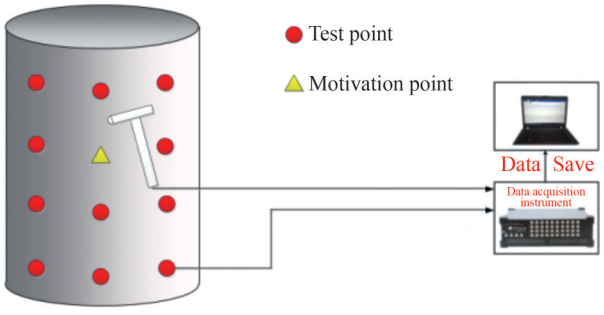

Figure 7 Schematic of the modal testing experiment

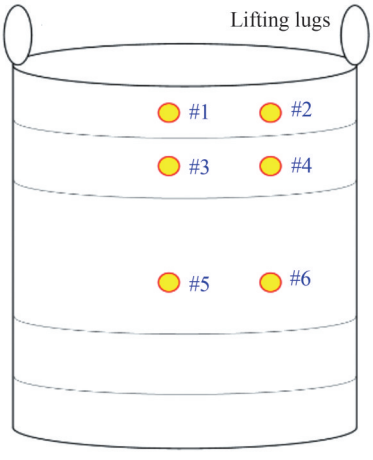

Figure 8 Measurement point in the experiment

(a) Modal testing of the laminated model (b) Modal testing of the steel model

Figure 9 Excitation applied to the model during the experiment

The structural boundary conditions should be free to avoid disturbance of structural vibration by external factors during the test. Therefore, the model should be kept in suspension by means of a lifting ring during the test. This way realizes the free boundary conditions of the model.

Computational modal analysis was conducted on the two models before the experiment to verify the rationality of the experimental scheme. The main methods for finite element modal analysis include the Block Lanczos method and the subspace method. The subspace method is appropriate for extracting fewer modes of large and medium-sized models and necessitates good element shapes when applied to solid and shell elements. For extracting a large number of modes from medium to large models, the Block method is more efficient due to its powerful functionality and is suitable for most modal problems. In models containing solid or shell elements, the Block method does not need to consider the initial truncation point and can handle rigid body modes effectively. However, it has higher memory space requirements. Given the regular shapes of the two models in the experiment, the subspace method was used for computational modal analysis.

In addition, considering that the load input frequency is not more than 20 000 Hz and the wave velocity of the stress wave in steel is 5 500 m/s, the minimum wavelength is not less than 0.28 m. In this work, the structural mesh is set to be 0.1 m, which indicates that the minimum number of structural units is included in one wavelength.

3.3 Equipment

In this experiment, the acceleration response of the model is collected using the acceleration sensor installed on the surface of the model. Moreover, a suitable test site must be provided to meet the requirements of lifting, lighting, loading, unloading, and other functions. A partial list of equipment is shown in Table 7.

Table 7 Experimental instruments

Test instrument	Number
086C03 force hammer (measuring range 25 kN, with pressure sensor, sensitivity 4 mV/N, resonant frequency > 20 Hz)	1
DH1A111E accelerometer (range 1 000 g, sensitivity 0.5 mV/g, L5 joint output, including 10 m line, magnetic seat)	>10
16-Channel Portable DHDAS 5920 Dynamic Signal Acquisition Instrument	1

The sampling frequency of the data acquisition instrument is set to 100 kHz, which can capture up to 10 000 Hz and can cover the first three orders of the intrinsic frequency of the model.

3.4 Experimental results

1) Verification of experimental scheme rationality.

The structural mode is determined by its inherent struc-

tural characteristics and is not influenced by the excitation force. To verify the rationality of the experimental scheme, excitations were applied to different points on the laminated structure, and the structural modal characteristics were measured accordingly.

The first three modal shapes and natural frequency distributions of the laminated structure under different excitation positions are shown in Table 8.

In the table, f represents the structural natural frequency; the subscripts 1, 2, and 3 indicate the order; "a" and "b" indicate two symmetric modes; "$_{\mathrm{I}}$" indicates incentive position 1; and "$_{\mathrm{II}}$" indicates incentive position 2. The modal test results show that the overall consistency of the modal vibration pattern is good before and after moving the excitation point. Differences exist in the amplitude of individual measurement points. The maximum shift of the intrinsic frequency is not more than 0.42%, which verifies the reasonableness of the test program.

Table 8 Comparison of modal test results at different excitation positions

Incentive position 1	Incentive position 2	Intrinsic frequency offset (%)
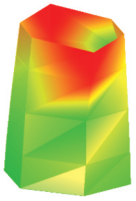	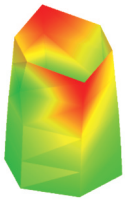	0.03
$f_{1aI} = 355.9$	$f_{1aII} = 356.0$	
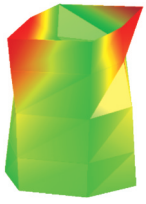		0.03
$f_{1bI} = 363.4$	$f_{1bII} = 363.3$	
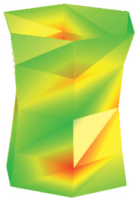	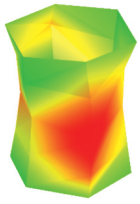	0.09
$f_{2aI} = 575.9$	$f_{2aII} = 575.4$	
	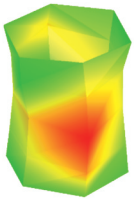	0.07
$f_{2bI} = 592.9$	$f_{2bII} = 593.3$	
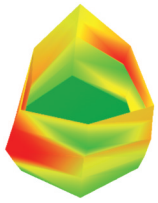	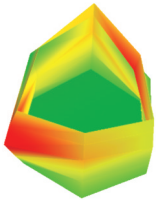	0.42
$f_{3aI} = 969.9$	$f_{3aII} = 965.8$	

2) Modal test results.

Based on the model tests, a FEM simulation solid calculation model with a scale of 1∶1 was established. The size of the solid mesh satisfies the requirement of having at least 6 elements per wavelength. The structural mesh consists of 202 830 elements, and the actual structure and the simulation model are shown in Figure 10. Given that the magnitude and location of external excitation are independent of the natural frequency and modal shape, no additional excitation forces need to be applied in the FEM modal calculations.

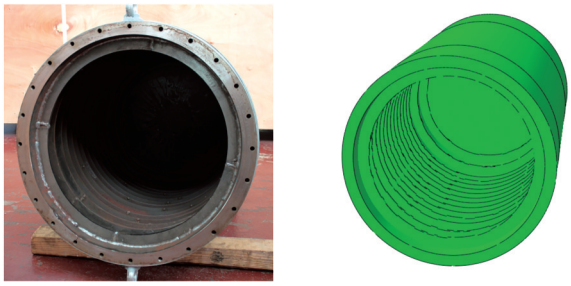

Figure 10 Actual structure and FEM simulation model

The test results of the laminated model using single-point excitation and multi-point pickup are compared with the modal calculation results of the finite element simulation model based on actual material properties and structural connection forms, as shown in Talbe 9. The modal shapes of the model are indicated by (m−n), where m is the axial half-wave number, and n is the circumferential half-wave number. In this way, a visual comparison of their modal shapes is provided.

The comparison of modal test results and simulation calculations shows that the maximum error of natural frequencies corresponding to the same modal shape obtained by the two modal analysis methods does not surpass 5.24%. This finding is similar to that obtained for common cylindrical structure modes. This similarity verifies the rationality and effectiveness of the experimental scheme.

The modal test results of the steel comparative model using single-point excitation and multi-point pickup are compared with the modal calculation results of the finite element simulation model, as shown in Table 10. The modal shapes of the structure are indicated by (m−n).

The comparison of modal test results and simulation calculations shows that the maximum error of natural frequencies corresponding to the same modal shape does not

Table 9 Modal comparison of the first three orders between simulation and experiment for the laminated model

Modal test results	Modal simulation results	Intrinsic frequency offset (%)
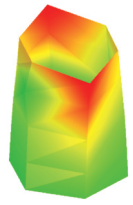 f = 356.0 (0–2)	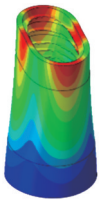 f = 353.8 (0–2)	0.62
 f = 363.3 (0–2 symmetry)	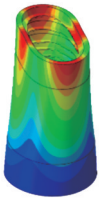 f = 354.1 (0–2 symmetry)	2.53
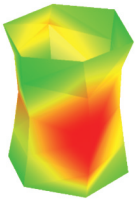 f = 575.4 (1–2)	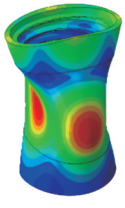 f = 594.9 (1–2)	3.39
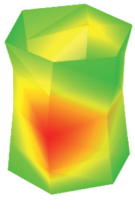 f = 593.3 (1–2 symmetry)	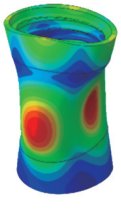 f = 595.3 (1–2 symmetry)	0.33
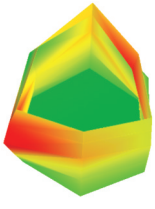 f = 965.8 (1–3)	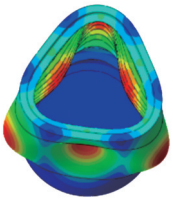 f = 915.2 (1–3)	5.24

surpass 4.24%. The modal shapes also exhibit a superposition of axial and circumferential half-waves, which verifies the effectiveness of the modal analysis methods. The error between the experimental and simulated values is due to the modeling process and disturbances in the testing process.

The modal comparison between the laminated structure and the steel structure is shown in Table 11. The modal frequency shift of the laminated model reaches 40.81% for m = 0, n = 2 mode and 15.89% for m = 1, n = 2 mode. The

Table 10 Modal comparison of the first three orders between simulation and experiment for steel model

Steel model test results	Steel model simulation results	Intrinsic frequency offset (%)
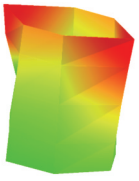 f = 214.66 (0–2)	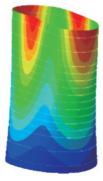 f = 208.09 (0–2)	3.06
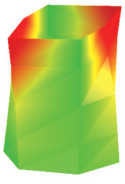 f = 215.04	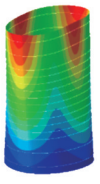 f = 208.10 (0–2)	3.23
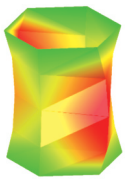 f = 510.60 (1–2)	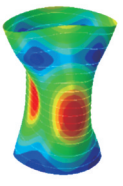 f = 498.98 (1–2)	2.28
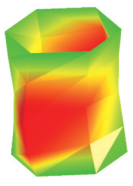 f = 513.80 (1–2 symmetry)	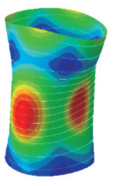 f = 498.99 (1–2 symmetry)	2.88
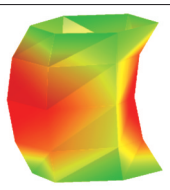 f = 677.00 (1–0)	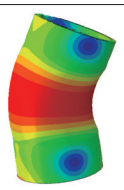 f = 680.60 (1–0)	0.53
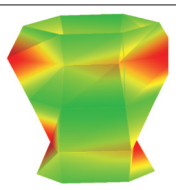 f = 1 010.50 (2–2)	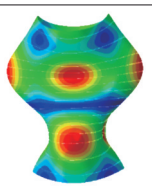 f = 1 044.90 (2–2)	3.46
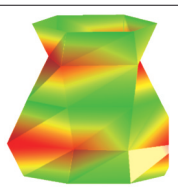 f = 1 018.00 (2–2 symmetry)	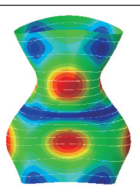 f = 1 044.90 (2–2 symmetry)	2.64

formula for calculating natural frequency indicates that the overall stiffness of the steel model is slightly lower than that of the laminated model under equal mass conditions. The carbon fiber material laid on the outer surface causes the natural frequencies of the steel model to shift to higher frequencies. This conclusion is consistent with the theoretical derivation in Section 2.3.

Table 11 Comparison of modal frequencies of cylinders with different structures

Modal order (m–n)	Laminated model intrinsic frequency (Hz)	Steel model intrinsic frequency (Hz)	Frequency shift (%)
(0–2)	356.0	214.66	39.70
(0–2 symmetry)	363.3	215.04	40.81
(1–2)	575.4	498.98	13.28
(1–2 symmetry)	593.3	498.99	15.89
(1–3)	965.8	–	–
(2–2)	–	1 010.50	–
(2–2 symmetry)	–	1 018.00	–

In addition, the modal shape differences between the laminated model and the steel model are significant. For example, the laminated model exhibits a unique triangular mode in the circumferential direction, whereas the steel model exhibits two orthogonal elliptical modes in the same frequency range. Therefore, the modal shapes of cylindrical structures with the same dimensions but different material properties differ greatly.

Considering that the model used in this study is the submarine segment, its aspect ratio is relatively small. Accordingly, its modal characteristics are breathing modes with large intrinsic frequencies. For the complete submarine structure, its modal characteristics are reflected in the "whip-like" form. This form has a relatively low intrinsic frequency, which mainly reflects low-frequency characteristics. The load frequency that causes the overall response of the submarine is generally low. Only the intrinsic frequency that is close to the load frequency needs to be analyzed in the study of the total structural strength and vibration characteristics. When the intrinsic frequency is migrated to a higher place, the modal response provoked by the original excitation force will be reduced. As a result, the overall structure is more secure under the same external force conditions.

3) Transfer function test results.

1) Comparison of different measurement points.

For the laminated model, measurement points #1, #3, and #5 were taken along the longitudinal direction of the model. The transfer functions of the model in the range of 1–1 200 Hz were measured, as shown in Figure 11.

In the figure, $H(w)$ denotes the transfer function. The comparison of the transfer function line spectrum in Figure 11 shows that significant peaks appear at 365 600,

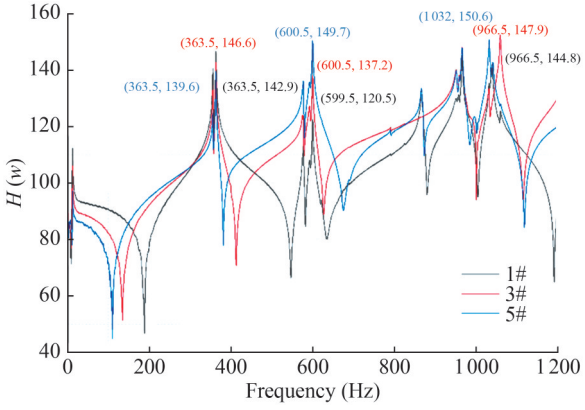

Figure 11 Comparison of transfer functions at different measurement points for laminated models

and 966 Hz at measurement point #1 near the open end, measurement point #3 at the transition ring, and measurement point #5 at the center of the structure. They are consistent with the natural frequencies obtained from the modal analysis, which verifies the effectiveness of this analysis method. Conversely, from the overall amplitude of the transfer function line spectrum, the overall vibration response at measurement point #5 at the center of the structure is larger than that at measurement point #1 near the open end, which is related to the structural form. The steel thickness at the open end is 34 mm, while the thickness at the center of the structure is 5 mm, which results in higher stiffness at the open end and greater vibration response at the center under unit excitation.

2) Comparison of different materials.

As shown in Equation (6), the amplitude of the transfer function $H(w)$ is related to the intrinsic frequency of the structure. When the frequency increases, $H(w)$ decreases. The comparison of the transfer function between the steel model and the laminated model is shown in Figure 12 and the quantitative comparison of the two is shown in Table 12.

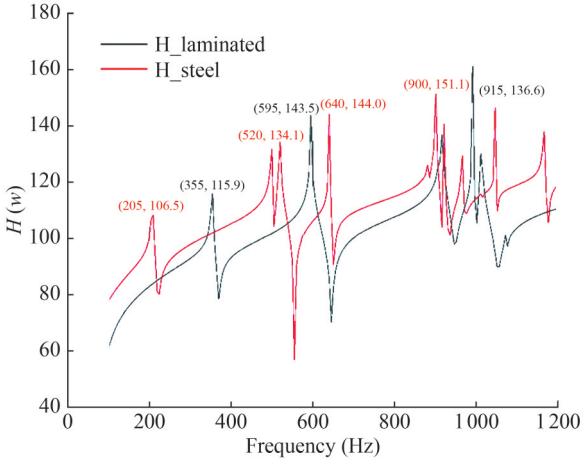

Figure 12 Comparison of transfer functions of laminated and steel models

Table 12 Comparison of transfer function data between steel and laminated models

Modal order	$H(w)$		
	Steel	Laminated	Reduction rate (%)
1	115.9	106.5	**8.11**
2	144.0	143.5	**0.35**
3	151.1	136.6	**9.60**

The comparison of the transfer function line spectrum of equal mass models with different material components in Figure 12 shows that the amplitudes of the transfer function for the steel model are generally higher than those of the laminated model. Therefore, the laminated structure made of steel and carbon fiber materials has better vibration-damping effects than the steel structure with equal mass. Meanwhile, the peak coordinates of the two curves correspond well to the natural frequencies obtained from modal analysis, which verifies the effectiveness of the analysis method. Therefore, replacing 40% of the steel thickness of the submarine shell with carbon fiber improves the structural damping characteristics by 9.6% while maintaining the same structural quality.

4 Damping characteristic analysis

The acceleration response of typical parts of the designed and processed laminated structure and the steel comparative structure with equal mass was tested using the hammering method. The loss factor values of the two structures were obtained using the transient decay method and compared.

4.1 Experimental principle

The internal loss factor is obtained through the transient decay method. The basic idea is to apply the Hilbert transform to the acceleration time-domain curve obtained from the experiment to obtain the envelope function of the structural response signal, which clearly reflects the relationship between signal amplitude and time decay. The slope of the envelope line is then calculated, which yields the damping ratio ξ. The internal loss factor η is obtained through the multiple relationship between the damping ratio and the internal loss factor. The specific method proceeds as follows:

The acceleration response signal of the structure after impact is obtained through experiments, and the Hilbert transform is applied to the signal:

$$\hat{a}(t) = H\left[a(t)\right] = a(t) \times \frac{1}{\pi t} = -\frac{1}{\pi}\int_{-\infty}^{+\infty} \frac{a(\tau)}{t-\tau} \mathrm{d}\tau \quad (7)$$

Its inverse transform is

$$a(t) = \hat{a}(t) \times \frac{1}{\pi t} = -\frac{1}{\pi}\int_{-\infty}^{+\infty} \frac{a(\tau)}{t-\tau} \mathrm{d}\tau \quad (8)$$

where $a(t)$ is the acceleration response of the structure after impact, and the symbol * denotes the convolution.

The analytic signal of the real function is obtained:

$$u(t) = a(t) + \mathrm{j}\hat{a}(t) \quad (9)$$

The plural expression for $u(t)$ is

$$u(t) = A(t)\mathrm{e}^{\mathrm{j}\theta t} \quad (10)$$

where $a(t) = \sqrt{a^2(t) + \hat{a}^2(t)}$. For the response signal $a(t)$ envelope, the instantaneous phase for the $\theta(t) = \arctan\left(\widehat{a}(t)/a(t)\right)$. Thus, any real function can be re-expressed as $a(t) = A(t)\cos(\theta)$. The response signal envelope to take the logarithm of the attenuation curve can be obtained. The absolute value of the slope of the curve for the damping ratio and the product of the center frequency of $\omega\xi$, which is divided by the center frequency of the damping ratio of ξ, is the average value of the loss factor (Inner Loss Factors, ILF) in the frequency band. Twice the damping ratio is the average value of Inner Loss Factors (ILF) in the frequency band, that is, $\eta = 2\xi$.

4.2 Test procedure

After the output of the test acquisition data, the usability of the data is first checked, and invalid data are eliminated. Then, the data are filtered, and the filtered data are processed according to the transient decay method to obtain the loss factor data. The sampling frequency was set to 100 kHz during the test. The flow of tests and the calculations are shown in Figures 13 and 14.

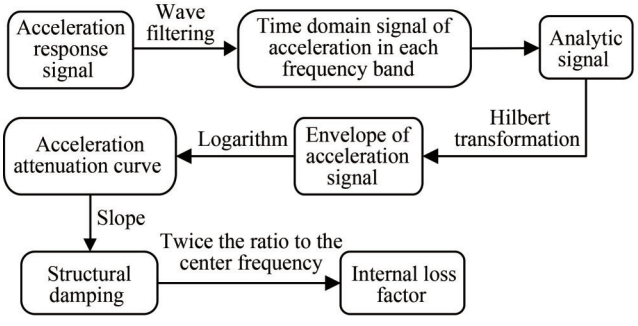

Figure 13 Data processing flow

4.3 Working condition settings

The experiment set up 10 measurement points, with 6 points on the middle section of the cylinder, 2 points on the transition section, and 2 points on the end faces. This test mainly focuses on #1–#6 test points, and #7–#10 points are set up to verify the reasonableness of the test.

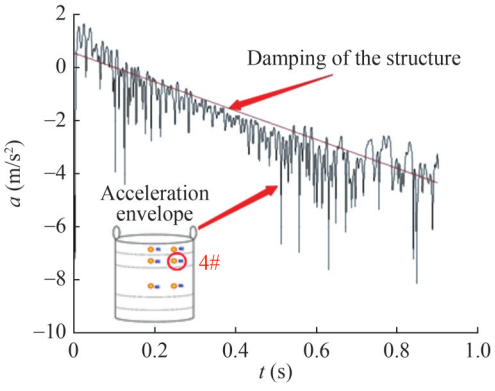

Figure 14 Attenuation curve of response signal

The experiment set up 9 excitation points, with 3 excitation points on the middle section, 4 on the transition section, and 2 on the ends. A force hammer was used to input excitation force during the experiment. The layout of measurement and excitation points is shown in Figure 15.

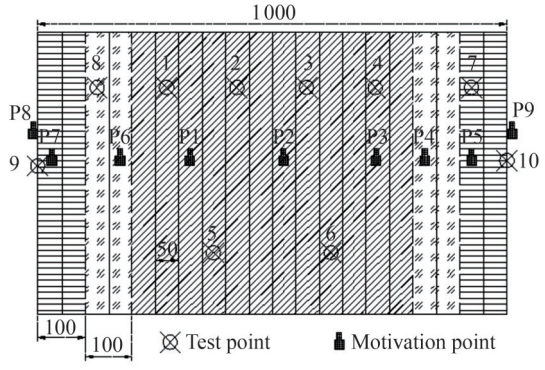

Figure 15 Test conditions and measurement points

4.4 Experimental results

The loss factors of the steel and laminated cylindrical middle sections obtained at each measurement point using the transient decay method are shown in Figure 16.

In Figure 16, Place$_i$ indicates the loss factor of the i-th test point. The average of each measurement point is shown by the dark red curve in the figure. As shown in Figure 16, the ILF values obtained at each measurement point exhibit a consistent trend. Similar amplitudes are observed in the high-frequency region, and slight fluctuations are found in the mid-low frequency region. Nevertheless, the fluctuations are insignificant.

Given that the structural loss factor is an inherent property, the amplitude is determined by material properties and geometric attributes and is independent of external loads. Therefore, the loss factors under each condition were averaged, and the results are shown in Figure 17. In the figure, P_i denotes the structural loss factor measured at the ith operating condition, and $P_{average}$ denotes the average of the loss factors measured at each operating condition.

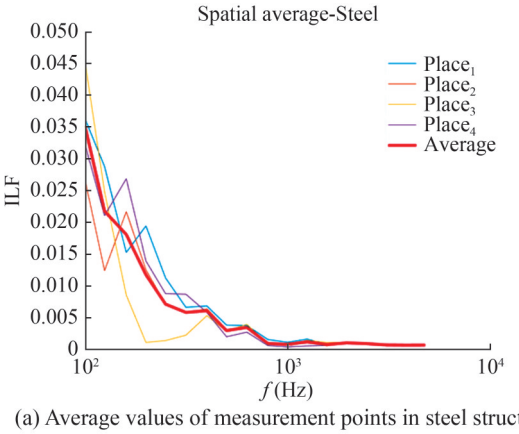

(a) Average values of measurement points in steel structures

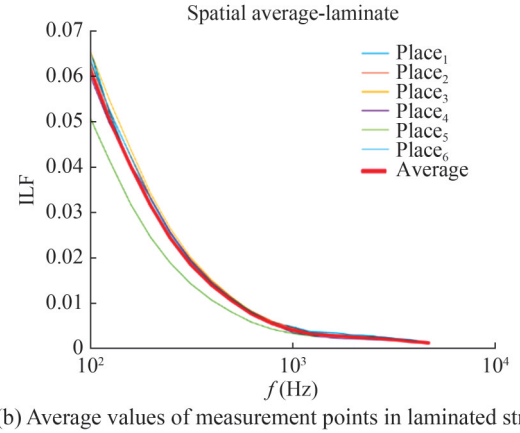

(b) Average values of measurement points in laminated structures

Figure 16 Structural loss factor measurement point average

The final average ILF values obtained for the steel-carbon laminated structure and the equal mass steel comparison model are shown in Table 13.

In Table 13, ILF_S denotes the ILF values for steel structures, and ILF_L denotes the ILF values for laminated structures. The table shows that the loss factor values of the laminated cylindrical shell structure are approximately 1.77–4.56 times those of the steel structure.

The data in the table are shown through bar and line charts, as shown in Figure 18, to more intuitively compare the ILF distribution of the two structures in each frequency band.

The abovementioned information suggests that, on the one hand, the loss factors of steel and laminated structures exhibit the characteristic of "large at low frequencies, small at high frequencies". The overall amplitudes range from 10^{-4}–10^{-2}, and the ILF values at each measurement point insignificantly differ. On the other hand, the loss factor of the laminated structure increases by approximately 1.77–4.56 times that of the steel structure, and the maximum loss factor improves to 1.77 times.

The ratio was plotted, as shown in Figure 19, to explore the variation in the loss factor ratio between the two models with the frequency band.

In Figure 19, the "ratio" value is the ratio of the loss factor of the laminated model to that of the steel model in the

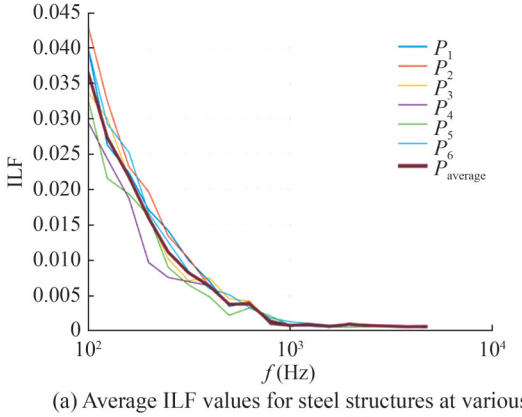

(a) Average ILF values for steel structures at various operating conditions

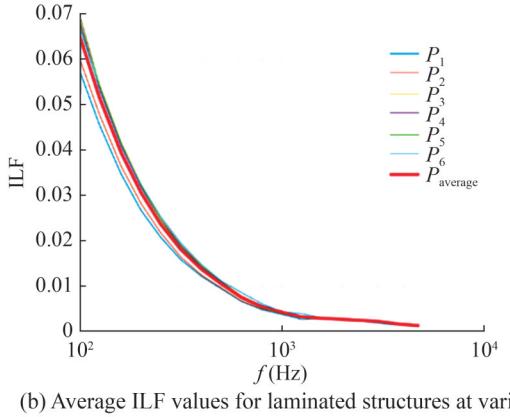

(b) Average ILF values for laminated structures at various operating conditions

Figure 17 Average values at various operating conditions

Table 13 Mean ILF values for both models in the full frequency band

Analysis frequency bands (Hz)	Mean value of ILF		Ratio (ILF_S/ILF_L)
	Steel structure	Laminated structure	
89.1–112	0.0649	0.0367	1.770
112–141	0.0514	0.0273	1.882
141z–178	0.0393	0.0217	1.808
178–224	0.0306	0.0159	1.920
224–282	0.0237	0.0111	2.126
282–355	0.0180	0.0082	2.198
355–447	0.0136	0.0063	2.153
447–562	0.0105	0.0038	2.770
562–708	0.0075	0.0038	1.967
708–891	0.0053	0.0014	3.892
891–1 120	0.0042	0.0012	3.459
1 120–1 400	0.0032	0.0009	3.492
1 400–1 750	0.0029	0.0006	4.558
1 750–2 195	0.0026	0.0009	2.855
2 195–2 745	0.0024	0.0008	3.144
2 745–3 420	0.0021	0.0007	3.146
3 420–4 260	0.0016	0.0006	2.619
4 260–5 350	0.0012	0.0006	1.963

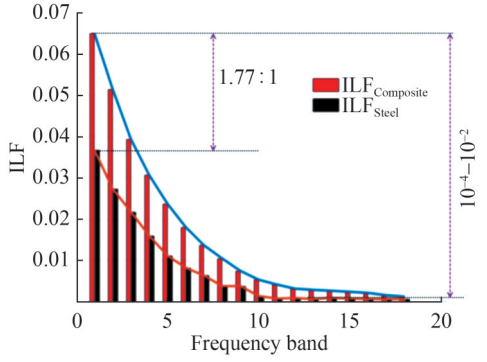

Figure 18 Comparison of the mean square values of ILF

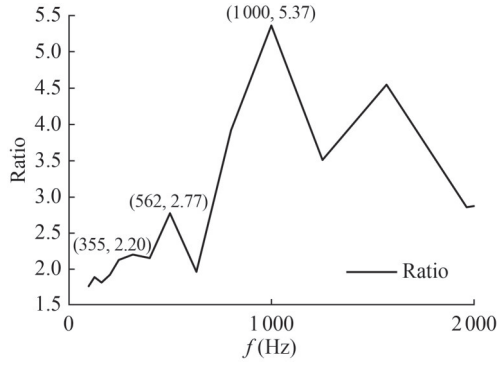

Figure 19 Variation in the ratio of the loss factor of the laminated model to that of the steel model with frequency

corresponding frequency band. The figure shows that the ratio of the loss factors of the two models peaks at 355, 562, and 1 000 Hz. This result indicates that the loss factor increases the fastest at the three frequencies after changing the structural material properties. Comparing the conclusions of the previous modal analysis suggests that the three frequencies correspond to the first three natural frequencies measured in the laminated model experiment. Therefore, the loss factor of the model increases the fastest at the shifted natural frequencies after the structural material properties are changed.

5 Conclusions

This study aims to improve the vibration and noise characteristics of submarines, balance the properties of the construction materials in terms of damping, strength, and stiffness, and control the manufacturing costs. Thus, in this study, a model of a laminated cylindrical shell made of steel and carbon fiber and a steel comparison model with equal mass and shape are designed based on the tectonics of the submersible segment. The modal and damping characteristics of the two models are compared and analyzed through experimentations and simulations. The following conclusions are obtained:

1) The relative error of the modal between experiment

and computation does not surpass 6%, which verifies the rationality of the modal analysis method.

2) The modal frequency shift of the laminated model reaches 40.81% in the $m = 0$, $n = 2$ mode and 15.89% in the $m = 1$, $n = 2$ mode, which provides a large modal avoidance space for the submarine design. This condition avoids intense resonance and effectively suppresses sound radiation caused by resonance.

3) The amplitudes of the transfer function for the steel model are generally higher than those of the laminated model. Up to a 9.6% reduction in the amplitude of the transfer function is observed, which means that the response of the laminated model provoked by the same excitation force will be lower than that of the steel model. Therefore, the vibration characteristics of the submarine have been improved.

4) Compared with that for the steel structure, the loss factor for the laminated structure of the same mass increases by approximately 1.77–4.56 times. The peak growth rate of the loss factor appears near the natural frequencies, which indicates that the laminated structures have better acoustic stealth capabilities.

Funding This study is supported by the National Science and Technology Major Project (J2019-1-0017-0016)

Competing interest The authors have no competing interests to declare that are relevant to the content of this article.

References

Amirabadi R, Ghazangian R (2018) A comprehensive study of an identical submarine subjected to explosion. International Journal of Coastal and Offshore Engineering 3(1): 21-34. http://doi.org/10.29252/ijcoe.2.1.21

Bakshi K, Chakravorty D (2014) First ply failure study of thin composite conoidal shells subjected to uniformly distributed load. Thin Walled Strucures 76: 1-7. https://doi.org/10.1016/j.tws.2013.10.021

Chen K, Dong JL (2023) Strength optimization design of spherical hulls for deep-sea submersibles: A hydraulic autofrettage approach in external pressure vessels. Ocean Engineering 287 (Part 2): 115853. https://doi.org/10.1016/j.oceaneng.2023.115853

Chen Y, Tong ZP, Hua HX, Wang Y, Gou HY (2009) Experimental investigation on the dynamic response of scaled ship model with rubber sandwich coatings subjected to underwater explosion. International Journal of Impact Engineering 36(2): 318-328. https://doi.org/10.1016/j.ijimpeng.2007.12.015

Cheng L, Wang C, Guo BB, Liang QY, Xie ZL, Yuan ZM, Chen XP, Hu HB, Du P (2024) Numerical investigation on the interaction between large-scale continuously stratified internal solitary wave and moving submersible. Applied Ocean Research 145: 103938. https://doi.org/10.1016/j.apor.2024.103938

Du Q, Cui W (2014) Stability analysis and experiment of large-scale spherical models built by high strength steel. Proceedings of the ASME 2014 33rd international conference on ocean. Offshore and Arctic Engineering. Volume 4B: Structures, Safety and Reliability. San Francisco: ASME V04BT02A014. https://doi.org/10.1115/OMAE2014-24056

Du QH (2017) Report on spherical pressure tests of 1# model of deep sea manned submarine. Shanghai: Shanghai Ocean University

Du QH, Liu W, Zou G, Qiu XY (2024) The reliability analysis and experiment verification of pressure spherical model for deep sea submersible based on data BP and machine learning technology. Marine Structures 96: 103635. https://doi.org/10.1016/j.marstruc.2024.103635

Feng GH, Zhu SH, Liu C, Chen W, Zhu Q, Xiao P (2024) Research on secondary low-velocity impact damage propagation in composite laminates. Aeronautical Computing Technique 54(6): 38-42

Fathallah E, Qi H, Tong LL, Helal M (2015) Design optimization of lay-up and composite material system to achieve minimum buoyancy factor for composite elliptical submersible pressure hull. Composite Structures 121: 16-26. https://doi.org/10.1016/j.compstruct.2014.11.002

Ghandehari MA, Masoodi AR, Hosseininia SES (2024) Multiscale dynamic behavior of imperfect hybrid matrix\fiber nanocomposite nested conical shells with elastic interlayer. Thin-Walled Structures 205 (Part B): 112494. https://doi.org/10.1016/j.tws.2024.112494

Ghandehari MA, Masoodi AR, Hosseininia ES (2025) Temperature-dependency and boundary condition impacts on the multiscale vibrational behavior of laminated nested dual conical shell structure semi-AUV applications. Applied Ocean Research 154: 104425. https://doi.org/10.1016/j.apor.2025.104425

Guo W, Dun CC, Marcus MA, Venturi V, Gainsforth Z, Yang FP, Feng XF, Viswanathan V, Urban JJ, Yu C, Zhang QY, Guo JH, Qiu JS (2023) The emerging layered hydroxide plates with record thickness for enhanced high-mass-loading energy Storage. Advanced Materials 35: 2211603. https://doi.org/10.1002/adma.202211603

Ismail MS, Mahmud J, Jailani A (2023) Buckling of an imperfect spherical shell subjected to external pressure. Ocean Engineering 275: 114118. https://doi.org/10.1016/j.oceaneng.2023.114118

Jiang G, Chen JC, Guo H, Wu G, Liu ZZ (2024) Study on local vibration control of the 100 m X-BOW polar exploration cruise ship. Applied Sciences 14(11): 4732. https://doi.org/10.3390/app14114732

Kandasamy R, Cui F, Townsend N, Foo CC, Guo J, Shenoi A, Xiong Y (2016) A review of vibration control methods for marine offshore structures. Ocean Engineering 127: 279-297. https://doi.org/10.1016/j.oceaneng.2016.10.001

Li HC, Pang FZ, Zhang H (2020) Analysis of free vibration characteristics of cylindrical shells with stepped thickness. Journal of Vibration Engineering 33(6): 1226-1233. http://doi.org/10.16385/j.cnki.issn.1004-4523.2020.06.014

Li C, Wang J, Qu Y, Zhang ZY, Hua HX (2016) Numerical and experimental investigation on vibro-acoustic response of a shaft-hull system. Engineering Analysis with Boundary Elements 71: 129-139. https://doi.org/10.1016/j.enganabound.2016.07.016

Liu JH, Wu YS, Zhao BL, Li YJ (2000) A simplified method for analyzing the response of GRP ship to underwater explosion. Journal of Ship Mechanics (3): 51-58

Lee GC, Kweon JH, Choi JH (2013) Optimization of composite sandwich cylinders for underwater vehicle application. Composite Structures 96: 691-697. https://doi.org/10.1016/j.compstruct.2012.08.055

Lopatin AV, Morozov EV (2015) Buckling of the composite sandwich cylindrical shell with clamped ends under uniform

external pressure. Composite Structures 122: 209-216. https://doi.org/10.1016/j.compstruct.2014.11.048

Ma G, He B, Liu JH, Zhang X, Chen H (2024) Research on the dynamics model of medium-weight impact testing for ship equipment. Shipbuilding of China 65(5): 222-232

McCoy RW, Sun CT (1997) Fluid-structure interaction analysis of a thick-section composite cylinder subjected to underwater blast loading. Composite Structures 37(1): 45-55. https://doi.org/10.1016/S0263-8223(97)00081-0

Messager T, Pyrz M, Gineste B, Chauchot P (2022) Optimal laminations of thin underwater composite cylindrical vessels. Composite Structures 58(4): 529-537. https://doi.org/10.1016/S0263-8223(02)00162-9

Moon CJ, Kim IH, Choi BH, Kweon JH, Choi JH (2010) Buckling of filament-wound composite cylinders subjected to hydrostatic pressure for underwater vehicle applications. Composite Structures 92(9): 2241-2251. https://doi.org/10.1016/j.compstruct.2009.08.005

Rezaiee-Pajand M, Masoodi AR (2019) Shell instability analysis by using mixed interpolation. Journal of the Brazilian Society of Mechanical Sciences and Engineering 41: article number 419. https://doi.org/10.1007/s40430-019-1937-y

Song GH, Zou YH, Nie Y, Habibi M, Albaijan I, Toghroli E (2024) Application of Hashin-Shtrikman bounds homogenization model for frequency analysis of imperfect FG bio-composite plates. Journal of the Mechanical Behavior of Biomedical Materials 151: 106321. http://doi.org/10.1016/j.jmbbm.2023.106321

Sun JG, Zou SM (2015) Vibration response analysis of an underwater submersible. Journal of Ship Mechanics 19(3): 303-310

Szturomski B, Kiciński R (2017) Simulation of the impact resistance of kilo type submarine loaded with non-contact mine explosion. Maritime Technical Journal 208(1): 99-110. http://doi.org/10.5602/0860889X.1237625

Tang YH, Gao C, Wang XR, Li HC, Pang FZ (2019) Study on acoustic radiation characteristics of composite material shell structures. Proceedings of 2019 Western China Acoustics Academic Exchange Conference. 65-68. DOI: 10.26914/c.cnkihy.2019.062384

Wang L, Ye C, Sun CQ, Feng SC, Xie XZ, Gao Y, Zhao K, Li YQ, Wan ZQ (2024a) Experiment investigation on compressive dwell fatigue behavior of titanium alloy pressure hull for deep-sea manned submersibles. Ocean Engineering 303: 117646. https://doi.org/10.1016/j.oceaneng.2024.117646

Wang ML, Chen Y, Gao WQ, Li Z, Zhang J (2024b) Theoretical and numerical study of the buckling of steel-composite cylindrical shells under axial compression. Applied Ocean Research 153: 104221. https://doi.org/10.1016/j.apor.2024.104221

Wang F, Zhang SJ, Yu S, Du QH, Zhang J, Jiang Z, Cui WC (2019) Design and analysis on a model sphere made of maraging steel to verify the applicability of the current design code. Ships Offshore Structure 14(1): 86-94. https://doi.org/10.1080/17445302.2018.1481627

Walker M, Smith RE (2003) A technique for the multiobjective optimisation of laminated composite structures using genetic algorithms and finite element analysis. Composite Structures 62(1): 123-128. https://doi.org/10.1016/S0263-8223(03)00098-9

Wu DT, Su JP, Chen F, Shi SK, Hua HX (2023) Analytical study on vibration behaviors of pump-jet–shaft–submarine hull system in wavenumber–frequency domain. Thin-Walled Structures 187: 110718. https://doi.org/10.1016/j.tws.2023.110718

Xie YY, Yu C, Ni L, Yu JH, Zhang YF, Qiu JS (2023) Carbon-hybridized hydroxides for energy conversion and storage: Interface chemistry and manufacturing. Advanced Materials 35(14): 2209652. http://doi.org/10.1002/adma.202209652

Xu HJ, Lv WJ, Zhou Y, Hu ZM, Zhang WJ (2011) Mechanical impedance characteristics analysis of deep diving vehicle pressure hull. Ship Science and Technology 33(1): 74-77. http://doi.org/10.3404/j.issn.1672-7649.2011.01.015

Xu ZY (2020) Lightweight design optimization of cylindrical shells under external hydrostatic. Wuhan: Huozhong University of Science & Technology

Yang ZY, Pang YJ, Wang J, Song L (2011a) Application of a response surface model in multi-objective optimization for submersible shapes. Journal of Harbin Engineering University 32(4): 407-410. http://doi.org/10.3969/j.issn.1006-7043.2011.04.002

Yang RY, SiMa C, Zhang JQ (2011b) Function analysis and hydrodynamic-performance design for the control rope fitted on the submersible. Journal of Ship Mechanics 15(Z1): 66-73

Yin L, Xu W, Fu J, Cheng G (2025) Multi-directional broadband vibration control of marine pipe systems using mistuned cyclic symmetric structure as dynamic vibration absorbers. Ocean Engineering 320: 120272. https://doi.org/10.1016/j.oceaneng.2024.120272

Yu H, Li CF, Ren HL, Lin Y (2011) Collision dynamic response research of a submersible. Journal of Harbin Engineering University 32(12): 1527-1533. http://doi.org/10.3969/j.issn.1006-7043.2011.12.001

Zhang RB, Li ZH, Sun QY, Yu GC, Wang XT, Wu LZ (2022) Design and characterization of the carton fiber tube reinforced polymer composite for full ocean depth submersibles. Composites Science and Technology 217: 109074. https://doi.org/10.1016/j.compscitech.2021.109074

Zhang N, Yu X, Ming FR (2021) Blast resistance of composite laminates in underwater multilayer protective structures. Acta Armamentarii 42(S1): 135-141

Zhang NL, Ma JJ, Wu L (2011) Research on the structure parameter feasible design region of deeper diving depth submarine pressure cylindrical shell . Ship Science and Technology 33(8): 16-19

Zhao SY, Liang S, Meng XS, Yan M (2025) Vibration and impact performance analysis of impact isolator of ship inertial navigation equipment. Machinery Design & Manufacture Online. https://doi.org/10.19356/j.cnki.1001-3997.20241121.004

Zhao HX (2023) Numerical simulation research on anti-knock performance of submersible composite dome. Harbin: Harbin Engineering University. http://doi.org/10.27060/d.cnki.ghbcu.2023.002503